LJMU Research Online

Li, Z, Wang, J, Shi, Z, Zhou, Y, Guo, J, Ren, X and Yang, Q

 Refinement mechanism of (Ti, Nb)(C, N) carbonitride in hypereutectic Fe-Cr-C-Ti-Nb-N coating by CeO2: A first principles study

http://researchonline.ljmu.ac.uk/id/eprint/14796/

Article

For more information please contact researchonline@ljmu.ac.uk

Refinement mechanism of (Ti, Nb)(C, N) carbonitride in hypereutectic Fe-Cr-C-Ti-Nb-N coating by CeO2: A first principles study

Zhengjun Li [a] , Jibo Wang [b], Zhijun Shi [a] , Yefei Zhou [a,c] , Jing Guo [d] , Xuejun Ren [d] , Qingxiang Yang [a, *]

[a] State Key Laboratory of Metastable Materials Science & Technology, Yanshan University, Qinhuangdao, 066004, PR China

[b] College of Physics and Mechanical & Electrical Engineering, Longyan University, Longyan, 364012, PR China

[c] College of Mechanical Engineering, Yanshan University, Qinhuangdao, 066004, PR China

[d] School of Engineering, Liverpool John Moores University, Liverpool, L3 3AF, UK

Abstract: The interface relationship between (Ti, Nb)(C, N) carbonitride and CeO2 was calculated by first-principles method. The mechanism that CeO2 as the nucleus of (Ti, Nb)(C, N) carbonitride in Fe-Cr-C-Ti-Nb-N coating was analyzed. The microstructure of the hypereutectic Fe-Cr-C-Ti-Nb-N-CeO2 coating was observed in this paper. The calculated results show that, by calculating the phonon dispersion curves and binding energy, the most stable structure of (Ti, Nb)(C, N) carbonitride is Ti3NbCN3. The two-dimensional lattice misfit between Ti3NbCN3(111) and CeO2(100) is 6.47 %, which indicates that CeO2 as nucleus of Ti3NbCN3 is medium-effective. The four interface structures (O-TiNb, O-CN, Ce-TiNb and Ce-CN) were established between Ti3NbCN3(111) plane and CeO2(100) plane, in which, the interface adhesive work of the O-TiNb interface is the largest, which is 7.66 J/m2, and its interfacial energy is the smallest, which is -0.82 J/m2. It indicates that this interface is stable from a thermodynamic point of view. The bond of the O-TiNb interface is mainly covalent. Therefore, CeO2 can be effective heterogeneous nucleus to refine Ti3NbCN3. The experimental results show that, the coarse primary M7C3 carbides are distributed on the matrix of hypereutectic Fe-Cr-C coating. By adding Ti, Nb, N elements and CeO2 to the coaing, CeO2 can be used as heterogeneous nucleus to refine Ti3NbCN3, and thus further refine the primary M7C3 carbides.

1. Introduction:

Hypereutectic Fe-Cr-C coating has been widely employed in the re-manufacturing field, because of its excellent abrasion resistance [1]. The primary M7C3 carbides are treated as the main strengthening phase in the hypereutectic Fe-Cr-C coating [2]. However, the coarse primary M7C3 carbides often crack and fall off from the coating surface during the service process, which causes the decrease of its abrasion resistance [3]. Consequently, in order to increase the service life, it is vital to refine the primary M7C3 carbides in the hypereutectic Fe-Cr-C coating. In recent years, many reports have been found that when Ti and Nb additives were added in the hypereutectic Fe-Cr-C coating, the dimensions of the primary M7C3 carbides were decreased, so that the abrasion resistance of the coating can be validly improved. Zhi et al. [4] studied the influence of

Nb additive on the microstructure and properties in Fe-Cr-C coating and found that NbC carbides formed in the molten pool can refines M7C3 carbides. Meanwhile, X. Zhi et al. [5,6] also reported the influence of Ti additive on the microstructure and properties in Fe-Cr-C coating, and found that TiC carbides are precipitated before M7C3 carbides and M7C3 carbides can be refined. However, Y.F. Zhou et al. [7] illustrated that if Ti and Nb contents in the coatings are too high, the elements Ti, Nb are combined with C to form (Ti, Nb)C carbides, while the C content in the matrix is significantly reduced. Subsequently, the volume fraction of the primary M7C3 carbide is significantly reduced, and even the hypereutectic Fe-Cr-C coating can be transformed into the hypoeutectic Fe-Cr-C one. Therefore, the abrasion resistance of the coating is seriously decreased too. In order to solve about problem, J.B. Wang et al. [8] added N additive in the hypereutectic Fe-Cr-C-Ti-Nb coating and concluded that the (Ti, Nb)(C, N) carbonitrides formed in the hypereutectic Fe-Cr-C-Ti-Nb-N coating can refine M7C3 carbides. Compared with Fe-Cr-C-Ti-Nb coating, the abrasion resistance of the hypereutectic Fe-Cr-C-Ti-Nb-N coating is furtherly increased.

The application of rare earth (RE) oxides in Fe-based coating has been attracted widespread attention [9,10]. H. Liu et al. [11] found that CeO2 is the nucleus of TiC during its heterogeneous nucleation when CeO2 is added into the hypereutectic Fe-Cr-C-Ti coating, which causes TiC refined and uniformly distributed. In consequence, the hypereutectic Fe-Cr-C-Ti coating with the primary M7C3 carbides can be further improved, and the service life of the coating is further perfected. H. Liu et al. [12] reported that when CeO2 was added into the hypereutectic Fe-Cr-C-Nb coating, CeO2 can be as the nucleus during the heterogeneous nucleation of NbC. So the NbC is refined, and then the primary M7C3 carbide is further refined. On the basis of the above work, we designed the hypereutectic Fe-Cr-C-Ti-Nb-*N*-CeO2 coating. However, does CeO2 have a refining effect on (Ti, Nb)(C, N) carbonitrides in the coating? What is the interface relationship between CeO2 and (Ti, Nb)(C, N) carbonitride? Because the dimensions both CeO2 and (Ti, Nb)(C, N) carbonitrides in hypereutectic Fe-Cr-C-Ti-Nb-N coating are very small, it is difficult to explain the refinement mechanism by experimental.

First-principles method has been widely used in material interface calculations, which can provide a basis for explaining the bonding properties between material interfaces. J. Yang et al. [13] researched the interface properties of Ag/SiC interface and Ag/TiC interface by the first principles method, and obtained the reason why Ag Cu Ti solder has good wettability on SiC ceramics. Q.R. Tian et al. [14] researched the bonding and electronic structures of the TiN–MnS/Fe interface structure by the first principles method, and found that Mn and Fe atoms can be sticked to the N-terminal TiN(111) plan in the form of face-centered cubic stacking, and an interface system can be formed when MnS and Fe grow on the TiN plane. J. Yang et al. [15] researched that there are both covalent and ionic bonds between Nb atoms and C, N atoms at NbC/NbN interface by the first principles method. The interface between Nb and N is more stable. X.Y. Jiao et al. [16] reported the γ-Fe/CeO2 heterogeneous nucleation interface for interface electronic structure, interface stability and bonding characteristics by first-principles calculation. They found that the O1-Fe interface energy is the lowest, while the ideal interface work of O2-Fe is the largest. An effective hetero-nucleation interface can be formed between γ-Fe and CeO2. The O1-Fe interface model is even better formed in

the beginning of hetero-nucleation. It's high for the bonding strength of O2-Fe interface, when two interface structures satisfy the formation conditions. However, the interface relationship between CeO2 and (Ti, Nb)(C, N) carbonitride by the first-principles calculation is reported rarely.

In present study, the mechanism that CeO2 as nucleus of (Ti, Nb)(C, N) carbonitride were investigated by first-principles calculation. The stable crystal structure of (Ti,Nb)(C,N) carbonitride was determined by calculating the phonon dispersion curves and binding energy. By two-dimensional lattice mismatch theory, the mismatch between CeO2 and (Ti, Nb)(C, N) carbonitride was calculated. The bulk properties, surface energy and adhesive strength, electronic model and bonding characteristics between CeO2 and (Ti, Nb)(C, N) carbonitrides were calculated. The bonding characteristics of heterogeneous nucleation interfaces were analyzed by electron localization function and partial density of states, which can theoretically express the mechanism of CeO2 as heterogeneous nucleus of (Ti, Nb)(C, N) carbonitrides. Finally, three kinds of hypereutectic Fe-Cr-C coatings (Fe–25Cr–4C–0.5Ti–0.5Nb, Fe–25Cr–4C–0.5Ti–0.5Nb-0.2 N and Fe–25Cr–4C–0.5Ti–0.5Nb-0.2 N- 0.2CeO2) were prepared and their microstructures were observed.

2. Calculational and experimental method

2.1. Calculation method In this paper, the first-principles calculation based on density functional theory was used to study the heterogeneous nucleation mechanism between CeO2 and (Ti, Nb)(C, N) carbonitride. The theoretical calculation was carried out by software of Vienna Ab-initio Simulation Package (VASP). The generalized gradient approximation (GGA-PBE) [17] exchange correlation function was used to process the selected particles, and the projection-embedded plane wave pseudopotential method [18] was used to deal with the interaction between the ion core and the valence electrons.

2.2. Experimental method According to the design composition of the coating, three kinds of hypereutectic Fe-Cr-C coatings (Fe–25Cr–4C, Fe–25Cr–4C–0.5Ti–0.5Nb- 0.2 N and Fe–25Cr–4C–0.5Ti–0.5Nb-0.2 N-2CeO2) were prepared by hardfacing method. Axiovert 200 MAT metallurgical microscope was used to observe the microstructure of the coating. D/max-2500/PC X-ray diffractometer was used to analyze the coating. Hitachi S3400 N field emission electron scanning electron microscope (FESEM) was used to collect and analyze the distribution of elements in the coating.

3. Calculational results

3.1. Stability prediction and VASP parameters determination

3.1.1. Stability of (Ti, Nb)(C, N) carbonitride The structure of CeO2 is usually stable. However, because (Ti, Nb)(C, N) carbonitride is composed of different Ti, Nb, C, N content, its structure is extremely complex and the content is uncertain. It is difficult to detect its true crystal structure by experimental. TiC, TiN, NbC, and NbN have the same crystal structure and similar lattice constants. Therefore, in this paper, TiC unit cell was taken as the basic crystal structure, in which, some Ti atoms are replaced by Nb atoms, and some C atoms are replaced by N atoms. Therefore, 19 crystal structures of (Ti, Nb)(C, N) carbonitride were designed and optimized by relaxation. It is one of the most commonly methods in physics to determine the stability of a structure by calculating its

phonon dispersion curves. If any virtual frequency is found on its phonon dispersion curves, it indicates that the structure is unstable [19]. The structural stabilities of 19 crystal structures of (Ti, Nb)(C, N) carbonitride were judged by calculating their phonon dispersion curves.

The calculation results show that, at 0 GPa, the phonon dispersion curves of Ti3NbCN3 unit cell and Ti3NbC3N unit cell don't show any virtual frequency, as shown in Fig. 1. Fig. 1(a) is the phonon dispersion curves of Ti3NbCN3 unit cell. Fig. 1(b) is the phonon dispersion curves of Ti3NbC3N unit cell. It indicates that, at 0 GPa, the structures of Ti3NbCN3 and Ti3NbC3N are stable. However, there are obvious virtual frequencies in the phonon dispersion curves of the remaining 17 structures, which indicates these structures are unstable. In addition, a more effective and concise method for evaluating structural stability is to calculate the binding energy of the structure. The binding energy is usually defined as the energy, which split a lattice structure into individual atoms. The lower the binding energy is, the more stable the structure is. The calculation equation is as follows [20]:

$$E_{coh} = \frac{1}{x+y+z+\dots}(E_{tot} - xE_{atom}^A - yE_{atom}^B - zE_{atom}^C - \dots) \qquad (1)$$

where $Ecoh$ is the total cell energy; x, y, z are the number of each atom contained in the unit cell; $E_{atom}^A, E_{atom}^B, E_{atom}^C$ are the energy of x, y, z atoms in the unit cell in the isolated state.

The binding energies of Ti3NbCN3 and Ti3NbC3N were calculated as -1.402 eV and -1.036 eV, respectively. It can be found that the binding energy of Ti3NbCN3 is lower than that of Ti3NbC3N, which indicates that the structure of Ti3NbCN3 is more stable than that of Ti3NbC3N. Therefore, in this paper, the structure of Ti3NbCN3 was selected as (Ti, Nb)(C, N) carbonitride to research the heterogeneous nucleation mechanism between CeO2 and (Ti, Nb)(C, N) carbonitride.

3.1.2. Crystal structure of CeO2 and Ti3NbCN3

The cell structures with CeO2 and Ti3NbCN3 are shown in Fig. 2. Fig. 2 (a) is the CeO2 structure with lattice parameters a = 5.411 Å. Fig. 2 (b) is the Ti3NbCN3 structure with lattice parameters a = 4.366 Å.

3.1.3. Determination of K-mesh and cut-off energy

Some parameters such as k-point and cut-off energy [21] in the Brillouin zone [22] during VASP calculation process need to be determined. The larger the selected k-point and cut-off energy values are, the more accurate of calculation result will be. However, it will cause the calculation amount to be increased and take a long time. Therefore, on the premise of ensuring the calculation accuracy, it is necessary to choose a value as small as possible to optimize the structure and improve the calculation efficiency.

The cut-off energy and k-points of CeO2 are shown in Fig. 3. Fig. 3(a) is the cut-off energy of CeO2. The system energy performed a gradually rise tendency before the cut-off energy value is set as 480 eV. Owing to the waveform tends to be flat after the cut-

off energy value is set as 480 eV, the cut-off energy of CeO2 is 480 eV. Fig. 3(b) is the k-points of CeO2. It can be seen that the energy of the system changes greatly before the k-points value is set as 7 × 7×7. When k-points value is set as 7 × 7×7, the system energy reaches convergence, and the curve tends to be smooth. Therefore, the k-points value of CeO2 is 7 × 7×7. The cut-off energy and k-points of Ti3NbCN3 are shown in Fig. 4. Fig. 4(a) is the cut-off energy of Ti3NbCN3. From Fig. 4(a), the system changes greatly before the cut-off energy value of Ti3NbCN3 is set as 500 eV. Due to the waveform tends to be flat after the cut-off energy value is set as 500 eV, the cut-off energy of Ti3NbCN3 is 500 eV. Fig. 4(b) is the k-points of Ti3NbCN3. It can be seen that the energy of the system changes greatly before the k-points value is taken as 10 × 10 × 10. When the k-points value is set as 7 × 7×7, the system energy reaches convergence, and the curve tends to be smooth. So the k-points value of Ti3NbCN3 is 10 × 10 × 10.

3.2. Bulk property of CeO2 and Ti3NbCN3

3.2.1. Bulk property of CeO2 The calculated bulk performance of CeO2 is shown in Fig. 5. Fig.5(a) is the band structure of CeO2. It can be seen that the conduction band has a long distance from the valence band. It's difficult for electrons to transition from the valence band to the conduction band because of the large band gap. Fig. 5(b) is the density of states of CeO2. It can be seen that there is almost no electron at the Fermi level, which indicates that CeO2 does not have metallic properties. From -5 eV to Fermi level, Ce-d orbital and O-p orbital both contribute to the density of states, and O-p orbital completely contains Ce-d orbital. The peak shapes and values of Ce-d orbital is similar to the O-p orbital at the range of -5 eV to 10 eV, which indicates a strong orbital hybridization exist at two atoms and forming covalent bond between them.

3.2.2. Bulk property of Ti3NbCN3

The calculated bulk performance of Ti3NbCN3 is shown in Fig. 6. Fig. 6(a) is the band structure of Ti3NbCN3. It can be seen that there are five high symmetry points X, R, M, G, R, and the bands that pass through the Fermi level, so the electrons easily transitions from the valence band to the conduction band, which indicates that Ti3NbCN3 has metallic properties. Fig. 6(b) is the density of states of Ti3NbCN3. It can be seen that there are electrons at the Fermi level, which is consistent with band structure. The peak shapes and values of Ti-d, Nb-d and C-p, N-p orbital are resembled at the range of -7 eV to -2 eV, which indicates a strong orbital hybridization exist between the two sets of atoms, then forming covalent bond between them. The bonding type of Ti3NbCN3 crystal structure is a mixture of covalent and metallic bonds.

3.3. Lattice mismatch Bramfitt two-dimensional lattice mismatch theory [23] can be applied to calculate the mismatch of different lattice planes of CeO2 and Ti3NbC3. The equation is as follows:

$$\delta_{(hkl)n}^{(hkl)s} = \sum_{i=1}^{3} \left[\left(\left| d_{[uvw]s}^{i} \cos\theta - d_{[uvw]n}^{i} \right| \Big/ d_{[uvw]n}^{i} \right) \Big/ 3 \right] \times 100\% \qquad (2)$$

where (*hkl*)*s* and (*hkl*)*n* are the lattice plane of nucleation substrate and nucleation phase; [*uvw*]*s* and [*uvw*]*n* are the direction of (*hkl*)*s* and (*hkl*)*n* ; *d*[*uvw*]*s* and *d*[*uvw*]*n*

are the interatomic spacing along [*uvw*]*s* and [*uvw*]*n*; θ is the angle between the directions of [*uvw*]*s* and [*uvw*]*n*.

The following conclusions needs to be emphasized according to the Bramfitt two-dimensional lattice mismatch theory: (i) as the lattice mismatch <6%, the nucleus substrate has a great effective to nucleus phases; (ii) as the lattice mismatch at 6%~12 %, the nucleus substrate has a moderately effective to nucleus phase; (iii) as the lattice mismatch > 12 %, the nucleus phase cannot be formed by attaching to nucleus substrate. Actually, when the lattice mismatch becomes smaller, the lattice of the nucleus substrate and the nucleus phase will match more closely.

The mismatches between the different crystal planes of Ti3NbCN3 and CeO2 are listed in Table 1. It reveals the interface mismatch between Ti3NbCN3(111) and CeO2(100) planes is the smallest, which is 6.09 %. It is moderately effective heterogeneous nucleus in the range of 6–12 %. Therefore, CeO2 meets the geometric conditions as the nucleus substrate of Ti3NbCN3.

3.4. Surface convergence test

Based on the calculation of the two-dimensional lattice mismatch and the crystal structure optimized by the bulk phase, the CeO2 (100) plane and the Ti3NbCN3 (111) plane were selected to establish the surface model. The different thicknesses and termination conditions of surface models are shown in Fig. 7. Fig. 7(a) is Ce-terminated model of CeO2 (100) plane. Fig. 7(b) is O-terminated model of CeO2 (100) plane. Fig. 7(c) is CN-terminated model of Ti3NbCN3 (111) plane. Fig. 7(d) is TiNb-terminated model of Ti3NbCN3 (111) plane. As the number of surface model layer increases, the characteristics of the surface structure gradually approach the bulk phase, and the calculation amount is also increased. In order to reduce the calculation amount and ensure the accuracy of the calculation, the surface convergence tests were performed on the surface models of CeO2 and Ti3NbCN3 to determine the minimum layer surface model that meets the accuracy requirements.

The number of internal anions and cations in CeO2 (100) plane and Ti3NbCN3 (111) plane are different. Therefore, the both constructed surfaces are polar surfaces, and the surface energy calculation equation is as follows:

$$\sigma = \frac{1}{2A}\left(E_{slab} - N_{Ce}\mu_{Ce}^{slab} - N_O\mu_O^{slab}\right) \tag{3}$$

$$\sigma = \frac{1}{2A}\left(E_{slab} - N_{Ti}\mu_{Ti}^{slab} - N_{Nb}\mu_{Nb}^{slab} - N_C\mu_C^{slab} - N_N\mu_N^{slab}\right) \tag{4}$$

where A is the surface area; *Eslab* is the calculated system energy of each atomic layer; *NCe* and *NO* are the quantity of Ce atoms and O atoms；*μslab Ce* and *μslab O* are the chemical potential of Ce atom and O atom; *NTi, NNb, NC* and *NN* are the quantity of Ti, Nb, C and N atoms in the surface model；μ_{Ti}^{slab}, μ_{Nb}^{slab}, μ_C^{slab}, μ_N^{slab} are the chemical potentials of Ti, Nb, C and N atoms.

In general, as the surface model is plenty relaxed, the particles in the system are stably distributed and reach equilibrium with the bulk phase. Therefore, it can be considered

that the surface model and the bulk phase is identical to the chemical potential. The equation for the chemical potential of the surface model is as follows:

$$\mu_{CeO_2}^{slab} = \mu_{CeO_2}^{bulk} = \mu_{Ce}^{slab} + 2\mu_O^{slab} \tag{5}$$

$$\mu_{Ti_3NbCN_3}^{slab} = \mu_{Ti_3NbCN_3}^{bulk} = 3\mu_{Ti}^{slab} + \mu_{Nb}^{slab} + 3\mu_C^{slab} + \mu_N^{slab} \tag{6}$$

where $\mu_{CeO_2}^{bulk}$ means the system energy of CeO2 after phase optimization;

$\mu_{Ti_3NbCN_3}^{bulk}$ is the system energy of Ti3NbCN3 after phase optimization.

According to the structure of Ti3NbCN3 unit cell, $N_{Ti} = 3N_{Nb}$, $N_C = 3N_N$. Calculating through Eqs. (3)–(6), the results calculated as follows:

$$\sigma = \frac{1}{2A}\left(E_{slab} - N_{Ce}\mu_{CeO_2}^{bulk} + (2N_{Ce} - N_O)\mu_O^{slab}\right) \tag{7}$$

$$\sigma = \frac{1}{2A}\left(E_{slab} - N_{Nb}\mu_{Ti_3NbCN_3}^{bulk} + (N_{Nb} - N_N)(3\mu_C^{slab} + \mu_N^{slab})\right) \tag{8}$$

For simplify calculations, the values can be approaching: $\mu_O^{slab} \approx \mu_O^{bulk}$, $\mu_C^{slab} \approx \mu_C^{bulk}$, $\mu_N^{slab} \approx \mu_N^{bulk}$. The surface energy of each termination surface was calculated with putting these values into Eqs. (7) and (8). Surface energies of the Ce-termination and O-termination model are listed in Table 2 and Table 3.

As listed in Table 2, for the Ce-terminated CeO2(100) surface model, when the number(N) of atomic layer is 11, the surface energy converges to 5.429 J/m2, and the surface model meets the convergence requirements. From Table 3, for the O-terminated CeO2 (100) surface model, when N is 7, the surface energy converges to 3.335 J/m2, and the surface model meets the convergence requirements. Therefore, the slabs values of 11 layers Ce-termination and the slabs values of 7 layers O-termination are used for the interface structure building.

The surface energies of TiNb-termination model and CN-termination model are listed in Tables 4 and 5. As listed in Table 4, for the TiNb- terminated Ti3NbCN3 (111) surface model, when N is 11, the surface energy converges to 0.219 J/m2, and the surface model meets the convergence requirements. From Table 5, for the CN-terminated Ti3NbCN3 (111) surface model, when N is 9, the surface energy converges to 0.361 J/m2, and the surface model meets the convergence requirements. Therefore, the slabs values of 11 layers TiNb-termination and the slabs values of 9 layers CN-termination are used to build the interface structure.

Concerning the slabs values of 11 layers of Ce-termination and 7 layers of O-termination are put into Eq. (7), the slabs values of 11 layers of TiNb-termination and 9 layers of CN-termination are put into Eq. (8). The simplified equation is as follows:

$$\sigma_{Ce-terminated-CeO_2} = \frac{1}{2A}\left(E_{\text{slab}} - 24\mu_{CeO_2}^{bulk} + 8\mu_O^{slab}\right) \tag{9}$$

$$\sigma_{O-terminated-CeO_2} = \frac{1}{2A}\left(E_{\text{slab}} - 12\mu_{CeO_2}^{bulk} - 8\mu_O^{slab}\right) \tag{10}$$

$$\sigma_{TiNb-terminated-Ti_3NbC_3N} = \frac{1}{2A}\left(E_{\text{slab}} - 12\mu_{Ti_3NbCN_3}^{bulk} + 2(3\mu_C^{slab} + \mu_N^{slab})\right) \tag{11}$$

$$\sigma_{CN-terminated-Ti_3NbC_3N} = \frac{1}{2A}\left(E_{\text{slab}} - 8\mu_{Ti_3NbCN_3}^{bulk} - 2(3\mu_C^{slab} + \mu_N^{slab})\right) \tag{12}$$

In practical terms, comparing the chemical potential of each atom in the bulk phase with that in the surface structure, it can be found that the chemical potential of each atom in the bulk phase is slightly larger than that in the surface structure. So, it can be further obtained as follows:

$$\Delta\mu_C = \mu_C^{slab} - \mu_C^{bulk} \leq 0 \Delta\mu_N = \mu_N^{slab} - \mu_N^{bulk} \leq 0 \tag{13}$$

$$\Delta\mu_O = \mu_O^{slab} - \mu_O^{bulk} \leq 0 \tag{14}$$

The equations of bulk energy are as follows:

$$\mu_{CeO_2}^{bulk} = \mu_{Ce}^{bulk} + 2\mu_O^{bulk} + \Delta H_{CeO_2} \tag{15}$$

$$\mu_{TiC}^{bulk} = 3\mu_{Ti}^{bulk} + \mu_{Nb}^{bulk} + 3\mu_c^{bulk} + \mu_N^{bulk} + \Delta H_{Ti_3NbCN_3} \tag{16}$$

Integrating Eqs. (9)–(16), it can be further obtained as follows:

$$\frac{1}{2}\Delta H_{CeO_2} \leq \mu_O^{slab} - \mu_O^{bulk} \leq 0 \tag{17}$$

$$\Delta H_{Ti_3NbCN_3} \leq \left(3\mu_C^{slab} + \mu_N^{slab}\right) - \left(3\mu_C^{bulk} + \mu_N^{bulk}\right) \leq 0 \tag{18}$$

According to the above calculations, the surface energy fluctuations of the CeO2 (100) plane and Ti3NbCN3 (111) plane are shown in Fig. 8. Fig. 8(a) is the relationship between the surface energy of the 11 layers Ce-terminated CeO2 surface model and the surface energy of the 7 layers O-terminated CeO2 surface model with the change of $\mu_O^{slab} - \mu_O^{bulk}$ chemical potential. Fig. 8(b) is the relationship between the surface energy of the 11 layers TiNb-terminated Ti3NbCN3 surface model and the surface energy of the 9 layers CN-terminated Ti3NbCN3 surface model with the change of $\left(3\mu_C^{slab} + \mu_N^{slab}\right) - \left(3\mu_C^{bulk} + \mu_N^{bulk}\right)$ chemical potential. It can be found that unlike the surface energy fluctuation curve of the CeO2(100) surface, in the surface energy fluctuation curve of the Ti3NbCN3(111) surface, the difference between the surface energy of TiNb termination surface and CN termination surface is small, and the fluctuation range is not changed much. Therefore, when the interface is constructed, two surface structures of TiNb termination and CN termination should be considered.

3.5. Interfacial property

3.5.1. Interface structure Based on the mismatch between Ti3NbCN3 and CeO2 and the surface convergence test, 11 layers of TiNb-terminated Ti3NbCN3(111) plane, 7 layers of CN-terminated Ti3NbCN3(111) plane, 11 layers of Ce-terminated CeO2(100)

plane and 7 layers O-terminated CeO2(100) plane were selected to build the interface. The schematic diagrams of four interface structures are illustrated in Fig. 9.

Fig. 9(a) and Fig. 9(a') are the Ce-CN interface structure and its vertical view. It can be seen that the Ce-terminated CeO2(100) plane and the CN-terminated Ti3NbCN3 (111) plane build the interface. Each Ce atom at the four apex angles corresponds with a N atom, and there is a Ce atom to the left and right corresponding to a C atom. There is an N atom in the center, a C atom above and below, and the remaining Ce atoms and C atoms are staggered along the x axis. Fig. 9(b) and Fig. 9(b') are the Ce-TiNb interface structure and its s vertical view. It can be seen that the Ce-terminated CeO2 (100) plane and the TiNb-terminated Ti3NbCN3 (111) plane build the interface. Each Ce atom at the four apex angles corresponds to a Nb atom, and a Ce atom both the left and right corresponds to a Ti atom. A Nb atom locates in the center, a Ti atom at the top and bottom, and the remaining Ce atoms and Ti atoms interlace along the x-axis arrangement. Fig. 9(c) and Fig. 9(c') are the O-CN interface structure and its vertical view. It can be seen that the O-terminated CeO2(100) plane and the CN-terminated Ti3NbCN3 (111) plane build the interface. In the four apex angles and the center, each O atom corresponds to an N atom, and each O atom at the top, bottom, left, and right corresponds to a C atom. The remaining O atoms and C atoms are staggered along the x axis. Fig. 9(d) and Fig. 9(d') are the O-CN interface structure and its vertical view. It can be seen that the O-terminated CeO2(100) plane and the TiNb-terminated Ti3NbCN3(111) plane build the interface. In the four apex angles and the center, each O atom corresponds to an Nb atom, and each O atom at the top, bottom, left, and right corresponds to a Ti atom, and the remaining O atoms and Ti atoms are staggered along the x axis.

3.5.2. Work of adhesion The interface adhesive work (*Wad*) of an ideal interface is defined as the reversible work on a unit area by separating an interface into two free surfaces. With increase of the *Wad*, the interface adhesive become perfect, and the interface stability become strong. The equation of the *Wad* is as follows [24]:

$$W_{ad} = \frac{1}{A}\left(E_{CeO_2} + E_{Ti_3NbC_3N} - E_{CeO_2/Ti_3NbCN_3}\right) \qquad (19)$$

where A is the interfacial area; E_{CeO2} is the total energy of CeO2(100) surface structure; $E_{Ti3NbC3N}$ is the total energy of Ti3NbCN3 (111) surface structure; $E_{CeO2/Ti3NbC3N}$ is the total energy of interface structure. According to Eq. (19), the ideal *Wad* of Ce-CN interface, Ce-TiNb interface, O-CN interface and O-TiNb interface are listed in Table 6. It can be seen from Table 6, that *Wad* of the four structures are as follows: WCe-TiNb < WCe-CN < WO-CN < WO-TiNb. The *Wad* of O-TiNb model is the largest, which is 7.66 J/m^2.

3.5.3. Interfacial energy

The interface energy (γ) is an important basis for judging the stability of the interface. The equation of γ is as follows [25]:

$$\gamma = \sigma_{CeO_2} + \sigma_{Ti_3NbCN_3} - W_{ad} \qquad (20)$$

where σCeO2 is surface energy of CeO2(100) surface model; σTi3NbCN3 is surface energy of Ti3NbCN3(111) surface model. According to Eq. (20), the γ of the four interfaces are listed in Table 7. It can be seen from Table 7, that the γ of the four structures are as follows: $\gamma_{\text{O-TiNb}} < \gamma_{\text{O-CN}} < \gamma_{\text{Ce-TiNb}} < \gamma_{\text{Ce-CN}}$. The γ of O-TiNb is the smallest, which is -0.82 J/m^2.

3.5.4. Interfacial electronic structure and bond characteristic

The charge density distributions of the (001) slices of CeO2(100)/ Ti3NbCN3 (111) interfaces are shown in Fig.10. Fig.10 (a) is the charge density distribution of the O-CN interface structure. After relaxation, the atomic misalignment occurs at the interface of the O and C and N atoms, and then the distances among atoms are reduced, which results the charge accumulation among atoms to form chemical bonds. Fig.10 (b) is the charge density distribution of the O-TiNb interface structure. Similar to the Fig.10 (a), after relaxation, the atoms on both sides of the interface move violently. O and Ti, Nb atoms produce atomic misalignment, and causes the inter-atomic distance decreased. There is a large amount of charge accumulation, and strong chemical bonds are formed. Fig.10 (c) is the charge density distribution of the Ce-CN interface structure. It is different from Fig.10 (a) and (b). After relaxation, as the atoms at the interface move extremely little, the distances among the atoms are large, and a small amount of charge accumulation appears, which make it difficult to form bonds. Fig.10 (d) is the charge density distribution of the Ce-TiNb interface structure. The atoms on both sides of the interface can hardly move after relaxation. The distances among the atoms are very large, and very little charge accumulation appears, so bonds is difficult to form.

The electronic structure of the interface can be studied by calculating the electron localization function (ELF) of the interface model. Combined with partial density of states (PDOS) to analyze the banding types. The equation of ELF is as follows [26]:

$$\text{ELF} = 1 \left/ \left[1 + \left(\frac{D_{(r)}}{Dh_{(r)}}\right)^2 \right] \right. \tag{21}$$

where D(r) means the real electron gas density; Dh(r) means the uniform electron gas density. The ELF values from 0 to 1 has three conditions as follows: (i) ELF =1, it corresponds to the fully localized state; (ii) ELF = 1/2, it corresponds to the uniform electron gas state; (iii) When ELF = 0, it corresponds to a completely delocalized state.

These ELF maps are the (001) slices of CeO2(100)/Ti3NbCN3 (111) interfaces are shown in Fig. 11. Fig. 11(a) is the ELF in the range of 0.3 to 0.8 between O atom and C or N atom, which indicates the covalent bond and ionic bond are the main bonding types at the interface. Fig11(b) is the ELF between O atom and Ti or Nb atom in the range of 0.3 to 0.4, which indicates the ionic bond is the main bonding type at the interface. Fig. 11(c) is the ELF between Ce atom and C or N atom in the range of 0.3 to 0.5, which indicates the ionic bond is the main bonding type at the interface. Fig. 13(d) is an area with an ELF of 0.5 between the interfaces. The electron gas is evenly distributed, and there may be metal bonds.

To further analyze the bonding types with the four interfaces, the PDOS of the four interfaces are shown in Fig. 12, in which, the Fermi level noted by dotted line.

Compared the atoms density of states in the first layer on both sides of the interface, it can be clearly seen that they are very different, which shows the localization characteristics of interfacial charge redistribution. Fig. 12(a) is the PDOS of several layers on both sides of the O-CN interface, It can be found that the similar waveforms from - 13 eV to - 9 eV appear among the O atom and C, N atoms orbits. Similarly, among the O atom and C, N atoms orbits, the same waveforms also appear from - 7 eV to 2 eV, and the orbital has obvious resonance. So it can be determined that the strong covalent, ionic and metal bonds exist in O-CN interface. Fig. 12(b) is the PDOS of several layers on both sides of the O-TiNb interface, in which, O atom and Ti, Nb atoms orbits have the similar waveforms from -5 eV to 2 eV, while the gravity center of the waveform is not consistent. So the O-TiNb interface is considered to exist ionic and metal bonds. Fig. 12(c) is the PDOS of several layers on both sides of the Ce-CN interface, in which, Ce atom and C, N atoms orbits have similar waveforms from - 9 eV to 8 eV. Ce atom and C, N atoms orbits have the similar waveform from 5 eV to 2 eV. It can be seen that ionic and metal bonds exist in O-CN interface. Fig. 12(d) is the PDOS of several layers on both sides of the Ce-TiNb interface. It can be seemed the PDOS waveform at the Ce-TiNb interface does not change much compared to the inside of the structure. There is only a small change from -2 eV to 1 eV, and there are some electrons at the Fermi level, which indicates the existence of metallic bonds. By comparing the PDOS of the four interface structures, it is obvious that the bond of the O-CN interface is the strongest.

4. Experimental results

4.1. Phase structures of the three coatings The XRD patterns of the three coatings are shown in Fig. 13, and they are calibrated and analyzed by comparing the standard PDF cards. It can be found that the main phases in the hypereutectic Fe-Cr-C coating are M7C3 carbide and γ-Fe. A new diffraction peak appears in the Fe-Cr-C-Ti- Nb-N coating, which is identified as the (Ti, Nb)(C, N) carbonitride. The main phase of the Cr-C-Ti-Nb-N-CeO2 coating is basically the same as that of the Fe-Cr-C-Ti-Nb-N coating, but the diffraction peak of CeO2 is not found, due to too little CeO2 additives.

4.2. Microstructure and element distribution maps of the three coatings

The microstructures of the coatings with three kind compositions are shown in Fig. 14. Fig. 14(a) is the microstructure of the hypereutectic Fe- Cr-C coating. It can be found that the coarse primary M7C3 carbides are distributed on the matrix with hexagon, whose sizes are about 100 μm. Fig. 14(b) is that of the hypereutectic Fe-Cr-C-Ti-Nb-N coating. From Fig. 14(b), when Ti, Nb and N elements were added in hypereutectic Fe-Cr-C coating, the primary M7C3 carbides are significantly refined, whose sizes are about 50 μm. Fig. 14(c) is that of the hypereutectic Fe-Cr-C-Ti- Nb-N-CeO2 coating. From Fig. 14(c), when CeO2 was added in hypereutectic Fe-Cr-C-Ti-Nb-N coating, the primary M7C3 carbides in the coating are further refined, whose sizes are about 10 μm.

The microstructure and element distribution maps of hypereutectic Fe-Cr-C-Ti-Nb-N-CeO2 coating are shown in Fig. 15. Fig. 15(a) is the microstructure of the coating. It can be seen that the light-colored polygons are M7C3 carbides, and there are black areas around them that are closely combined with it. Fig. 15(b) is the distribution map of element Cr, and the area of accumulation is consistent with the distribution area of

M7C3 carbide in Fig. 14(a), which indicates that M7C3 carbide is a Cr-rich one. Fig. 15(c)-(f) are the distribution maps of the elements Ti, Nb, C, and N, respectively. Elements clustered in several pictures, which are consistent with the distribution of the black area in Fig. 15 (a). Combined with X-ray diffraction analysis, it is determined that they are (Ti, Nb)(C, N) carbonitrides. It shows that (Ti, Nb)(C, N) carbonitrides as heterogeneous nucleus to refine M7C3 carbide. In Fig. 15(g), the distribution of element Ce was measured, and it is found that element Ce aggregates in (Ti, Nb)(C, N) carbonitrides. It indicates that CeO2 as heterogeneous nucleus can refine (Ti, Nb)(C, N) carbonitrides.

5. Conclusion

(1) By calculating the phonon dispersion curves and binding energy, the most stable crystal structure of (Ti, Nb)(C, N) carbonitride is Ti3NbCN3. (2) The interface mismatch between Ti3NbCN3(111) and CeO2(100) planes is the lowest, which is 6.09 %. The interface between CeO2 and Ti3NbCN3 is a semi-coherent interface, which is a moderately effective heterogeneous nucleus in the range of 6–12 %. (3) The surface energy of Ce-terminated converges to 11 layers with a surface energy of 5.429 J/m2. The surface energy of O-terminated converges to 7 layers with a surface energy of 3.335 J/m2. The surface energy of TiNb-terminated converges to 11 layers with a surface energy of 0.219 eV. The surface energy of CN-terminated converges to 7 layers with a surface energy of 0.361 eV. (4) The Ce-CN interface structure and the Ce-TiNb interface structure have smaller interface adhesive work and larger interfacial energy, and the interface structures are unstable. The O-CN interface and the O-TiNb interface have larger interface adhesive work and smaller interfacial energy, and the interface combination status of the two structures are better. Among them, the O-TiNb interface structure is the most stable, and the interface bonding type is mainly covalent bonds. (5) The experimental results show that in Fe-Cr-C-Ti-Nb-N-CeO2 coating, CeO2 can be used as heterogeneous nucleus to refine (Ti, Nb)(C, N) carbonitride, and thus further refine the primary M7C3 carbides.

Declaration of Competing Interest The authors report no declarations of interest.

References

[1] X.J. Wu, J.D. Xing, H.G. Fu, X.H. Zhi, Effect of titanium on the morphology of primary M7C3 carbides in hypereutectic high chromium white iron, Mater. Sci. Eng. A 457 (2007) 180–185.

[2] V.E. Buchanan, P.H. Shipway, D.G. McCartney, Microstructure and abrasive wear behaviour of shielded metal arc welding hardfacings used in the sugarcane industry, Wear 263 (2007) 99–110.

[3] X.H. Zhi, J.D. Xing, Y.M. Gao, H.G. Fu, J.Y. Peng, B. Xiao, Effect of heat treatment on microstructure and mechanical properties of a Ti-bearing hypereutectic high chromium white cast iron, Mater. Sci. Eng. A 487 (2008) 171–179.

[4] X. Zhi, J. Xing, H. Fu, Effect of niobium on the as-cast microstructure of hypereutectic high chromium cast iron, Mater. Lett. 62 (6-7) (2008) 857–860.

[5] X. Zhi, J. Xing, Y. Gao, Effect of heat treatment on microstructure and mechanical properties of a Ti-bearing hypereutectic high chromium white cast iron, Mater. Sci. Eng. A 487 (1-2) (2008) 171–179.

[6] X. Zhi, J. Xing, H. Fu, Effect of titanium on the as-cast microstructure of hypereutectic high chromium cast iron, Mater. Charact. 59 (9) (2008) 1221–1226.

[7] Y.F. Zhou, Y.L. Yang, J. Yang, F.F. Hao, D. Li, X.J. Ren, Q.X. Yang, Effect of Ti additive on (Cr, Fe)7C3 carbide in arc hardfacing layer and its refined mechanism, Appl. Surf. Sci. 258 (2012) 6653–6659.

[8] J.B. Wang, T.T. Liu, Y.F. Zhou, X.L. Xing, S. Liu, Y.L. Yang, Q.X. Yang, Effect of nitrogen alloying on the microstructure and abrasive impact wear resistance of Fe-Cr-C-Ti-Nb hardfacing alloy, Surf. Coat. Tech. 309 (2017) 1072–1080.

[9] Y.W. Kim, Y.S. Chun, T. Nishimura, M. Mitomob, Y.H. Lee, High-temperature strength of silicon carbide ceramics sintered with rare-earth oxide and aluminum nitride, Acta Mater. 55 (2007) 727–736.

[10] T. Mori, D.R. Ou, J. Zou, J. Drennan, Present status and future prospect of design of Pt–cerium oxide electrodes for fuel cell applications, Prog. Nat. Sci-Mater 22 (2012) 561–571.

[11] H. Liu, X.L. Xing, L.X. Rao, Z.J. Shi, S. Liu, Yefei Zhou, Q.X. Yang, Interface relation between CeO2/TiC in hypereutectic Fe-Cr-C-Ti-CeO2 hardfacing alloy, Matre. Chem. Phys. 222 (2019) 181–192.

[12] H. Liu, X.M. Yuan, L.X. Rao, S. Liu, Z.J. Shi, Yefei Zhou, Q.X. Yang, Refinement mechanism of NbC by CeO2 in hypereutectic Fe-Cr-C hardfacing coating, J. Alloy. Comp. 770 (2019) 1016–1208.

[13] J. Yang, Z. Ye, J.H. Huang, S.H. Chen, Y. Zhao, First-principles calculations on wetting interface between Ag-Cu-Ti filler metal and SiC ceramic: Ag (111)/SiC (111) interface and Ag (111)/TiC (111) interface, Appl. Surf. Sci. 462 (2018) 55–64.

[14] Q.R. Tian, J. Li, X.Y. Wu, J.X. Fu, G.C. Wang, Growth mechanism of MnS/Fe on TiN surface: first principle investigation, J. Alloy. Comp. (2020).

[15] J. Yang, J.H. Huang, D.Y. Fan, S.H. Chen, First-principles investigation on the electronic property and bonding configuration of NbC (111)/NbN (111) interface, J. Alloy. Comp. 689 (2016) 874–884.

[16] X.Y. Jiao, W.T. Fu, Z.J. Shi, Z.J. Li, Y.F. Zhou, X.L. Xing, Z.R. Wang, Q.X. Yang, First principles investigation on interface properties and formation mechanism of γ-Fe/CeO2 heterogeneous nucleation interface, J. Alloy. Comp. (2020), 154867.

[17] J.P. Perdew, K. Burke, M. Ernzerhof, Generalized gradient approximation made simple, Phys. Rev. Lett. 77 (1996) 3865–3868.

[18] P.E. Blochl, Projector augmented-wave method, Phys. Rev. B 50 (1994) 17953–17979.

[19] L.G. Wang, P. Kratzer, M. Scheffler, et al., Formation and stability of self-assembled coherent islands in highly mismatched heteroepitaxy, Phys. Rev. Lett. 82 (1999) 4042–4045.

[20] J.H. Hildebrand, Solubility, J. Am. Chem. Soc. 38 (1916) 1452–1473.

[21] N. Troullier, J.L. Martins, Efficient pseudopotentials for plane-wave calculations, Phys. Rev. B 43 (1991) 1993–2006.

[22] H.J. Monkhorst, J.D. Pack, Special points for Brillouin-zone integrations, Phys. Rev. B 13 (1976) 5188–5192.

[23] Z.M. Xu, G.F. Liang, Q.F. Guan, Q.C. Jiang, TiC as heterogeneous nuclei of the (Fe, Mn)3C and austenite intergrowth eutectic in austenite steel Matrix wear resistant composite, Mater. Res. Bull. 39 (2004) 457–463.

[24] X.B. Zhao, J. Zhang, S. Liu, C.C. Zhao, C.X. Wang, X.J. Ren, Q.X. Yang, Investigation on grain refinement mechanism of Ni-based coating with LaAlO3 by first-principles, Mater. Design 110 (2016) 644–652.

[25] Z.J. Shi, S. Liu, Y.K. Gao, Y.F. Zhou, X.L. Xing, X.J. Ren, Q.X. Yang, Mechanism of Y2O3 as heterogeneous nucleus of TiC in hypereutectic Fe-Cr-C-Ti-Y2O3 coating: first principle calculation and experiment research, Mater. Today Commun. 13 (2017) 80–91.

[26] A. Becke, K. Edgecombe, A simple measure of electron localization in atomic and molecular systems, J. Chem. Phys. 92 (1990) 5397–5403.

Table 1
Lattice mismatch of CeO_2 and Ti_3NbCN_3.

Matching face	(100)Ti₃NbCN₃ // (100)CeO₂ //			(110)Ti₃NbCN₃ // (100)CeO₂ //			(111)Ti₃NbCN₃ // (100)CeO₂ //			(100)Ti₃NbCN₃ // (110)CeO₂ //			(110)Ti₃NbCN₃ // (110)CeO₂ //			(111)Ti₃NbCN₃ // (110)CeO₂ //		
[uvw]Ti₃NbCN₃	[010]	[001]	[011]	[001]	[1̄10]	[1̄11]	[1̄10]	[11̄2]	[3̄1̄2]	[010]	[001]	[011]	[001]	[1̄10]	[1̄11]	[1̄10]	[11̄2]	[20̄2]
[uvw]CeO₂	[1̄10]	[011]	[010]	[010]	[001]	[011]	[010]	[001]	[011]	[001]	[1̄10]	[11̄2]	[1̄10]	[001]	[1̄10]	[001]	[1̄10]	[11̄2]
θ(°)	0	0	0	0	0	9.736	0	0	4.107	0	0	4.107	0	0	0	0	0	0
dTi₃NbCN₃ (Å)	4.365	4.365	6.174	4.365	6.174	7.561	6.174	5.347	8.167	4.365	4.365	6.174	4.365	6.174	7.561	6.174	5.347	5.629
dCeO₂(Å)	3.859	3.859	5.458	5.458	5.458	7.719	5.458	5.458	7.719	5.458	3.859	6.685	3.859	5.458	6.685	7.719	5.458	8.167
δ(%)	11.59 %			12.42 %			6.47 %			14.08 %			11.59 %			14.10 %		9.454

Table 2

Calculated surface energy of CeO$_2$ (100) Ce-terminated models.

Layer(N)	3	5	7	9	11	13
Surface energy(J/m^2)	6.015	6.013	5.539	5.495	5.429	5.417

Table 3

Calculated surface energy of CeO$_2$ (100) O-terminated models.

Layer(N)	3	5	7	9	11
Surface energy(J/m^2)	3.328	3.348	3.335	3.334	3.335

Table 4

Calculated surface energy of Ti$_3$NbCN$_3$ (111) TiNb-terminated models.

Layer(N)	3	5	7	9	11	13
Surface energy(J/m^2)	0.233	0.224	0.226	0.223	0.219	0.220

Table 5

Calculated surface energy of Ti$_3$NbCN$_3$ (111) CN-terminated models.

Layer(N)	3	5	7	9	11
Surface energy(J/m^2)	0.369	0.371	0.365	0.361	0.362

Table 6

W_{ad} of CeO$_2$ (100)/ Ti$_3$NbCN$_3$ (111) models.

Interface	Ce-CN	Ce-TiNb	O-CN	O-TiNb
W_{ad} (J/m^2)	3.48	0.27	6.33	7.66

Table 7

γ of CeO$_2$ (100)/ Ti$_3$NbCN$_3$ (111) models.

Interface	Ce-CN	Ce-TiNb	O-CN	O-TiNb
γ (J/m^2)	7.73	8.66	2.78	−0.82
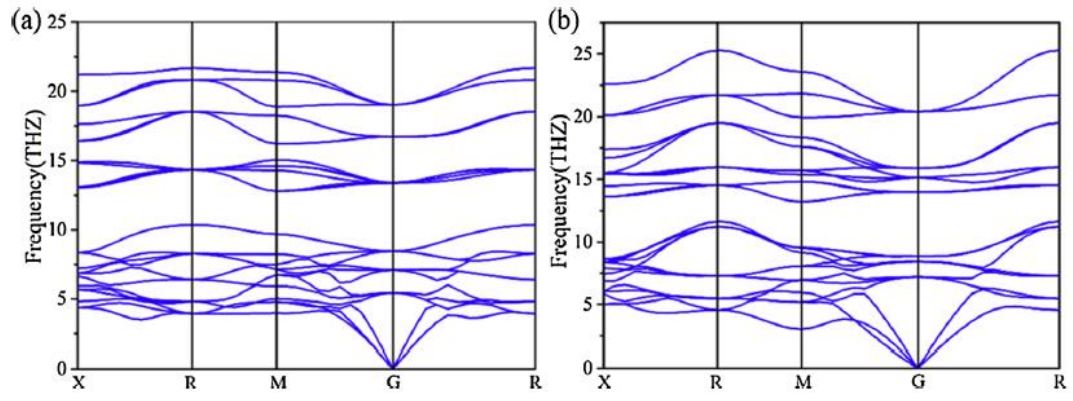
Fig. 1. Phonon dispersion curves of Ti3NbCN3 and Ti3NbC3N unit cell structure. (a) Ti3NbCN3; (b) Ti3NbC3N.
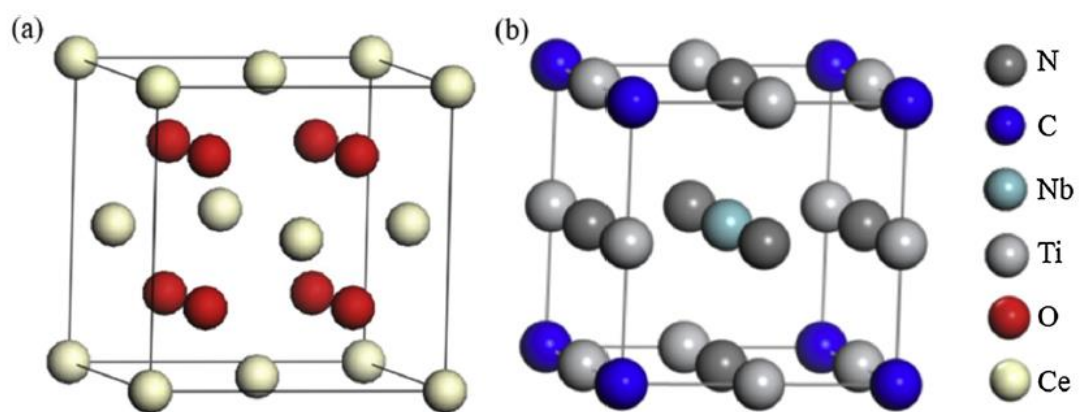
Fig. 2. Structure of CeO2 and Ti3NbCN3. (a) CeO2; (b) Ti3NbCN3
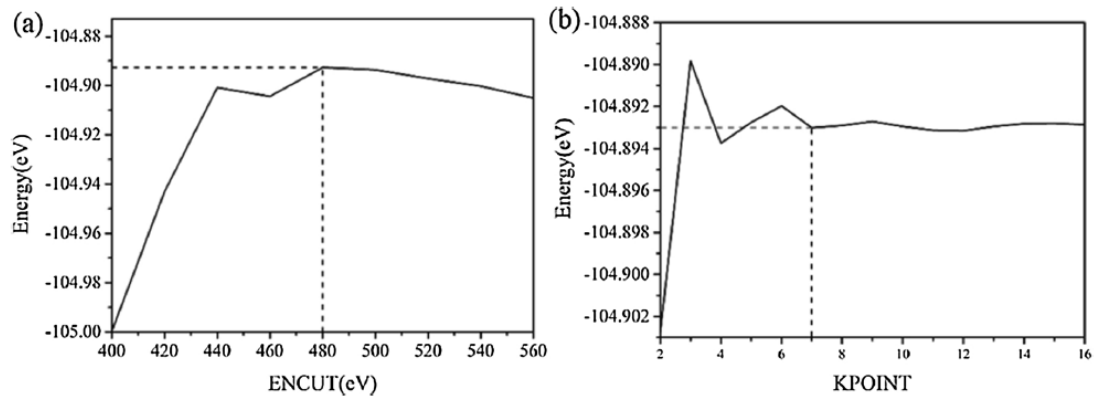
Fig. 3. Determination of cut-off energy and k-points of CeO2. (a) cut-off energy; (b) k-points.
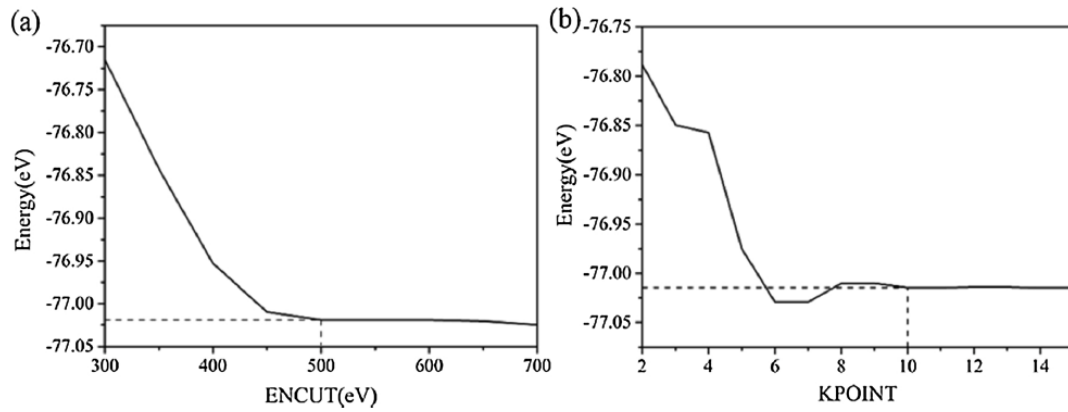
Fig. 4. Determination of cut-off energy and k-points of Ti3NbCN3. (a) cut-off energy; (b) k-points.
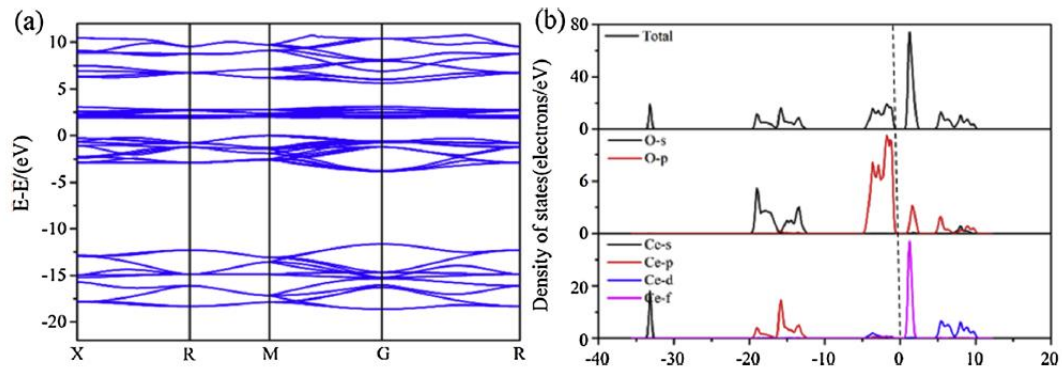
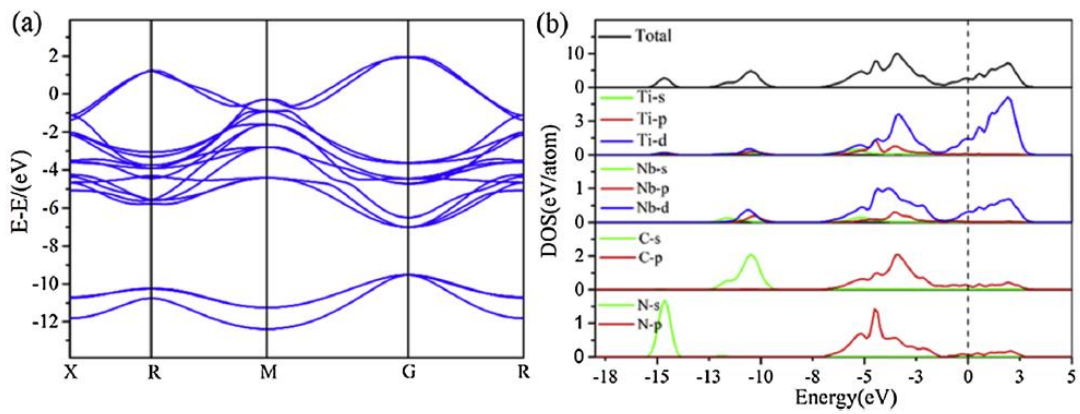**Fig. 5.** Band structure and density of states of CeO2. (a) Band structure; (b) Density of states.

Fig. 6. Band structure and density of states of Ti3NbCN3. (a) Band structure; (b) Density of states.
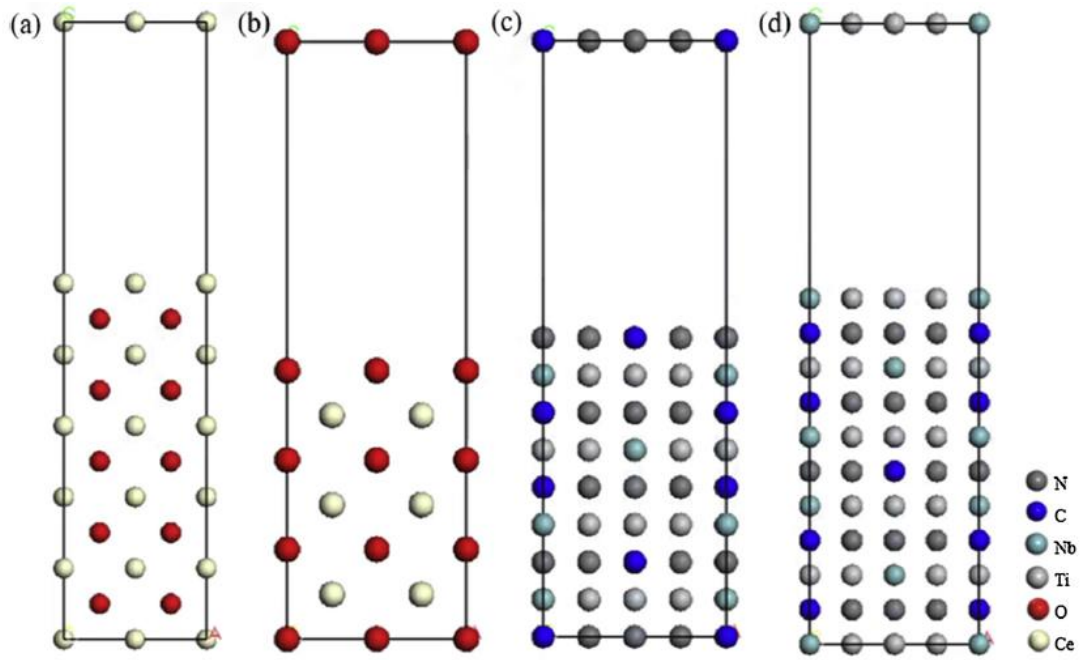
Fig. 7. Schematic diagrams of CeO2 and Ti3NbCN3 surface models. (a) CeO2 (100) Ce-terminated model; (b) CeO2 (100) O-terminated model; (c) Ti3NbCN3 (111) CN-terminated model; (d) Ti3NbCN3 (111) TiNb-terminated model.
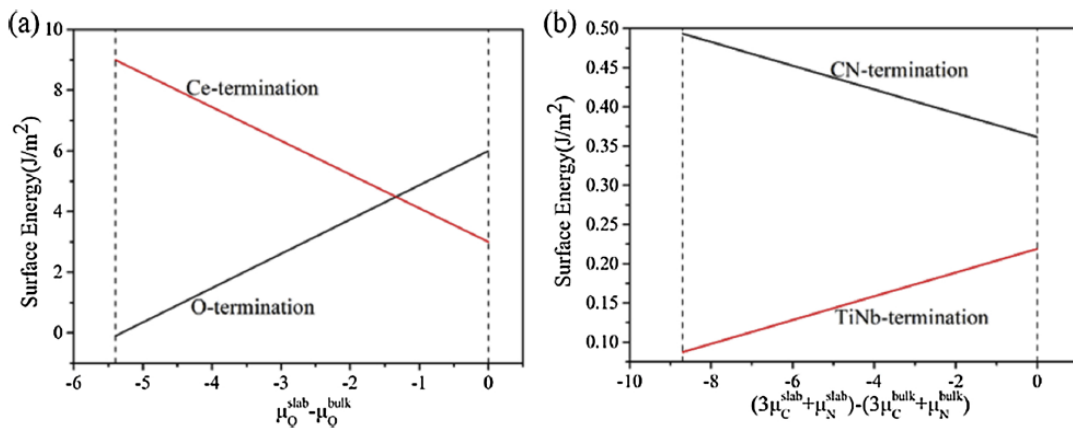
Fig. 8. Surface energy fluctuation. (a) CeO2(100); (b) Ti3NbCN3 (111).
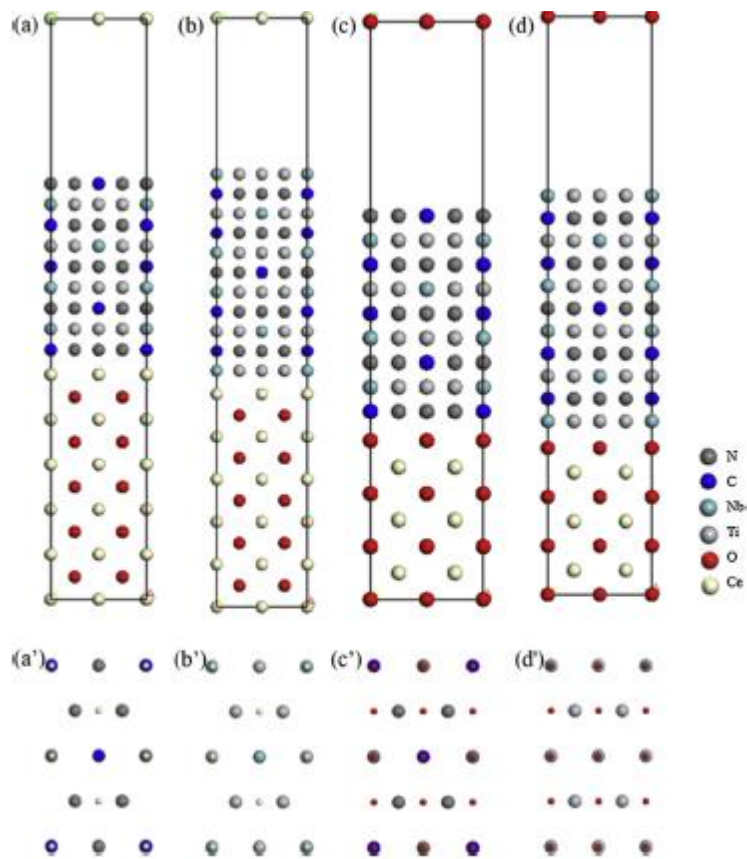
Fig. 9. Four interface structures and their top views. (a,b) Ce-CN interface structure and its top view; (c,d) Ce-TiNb interface structure and its top view; (e,f) O-CN interface structure and its top view; (g,h) O-TiNb interface structure and its top view.
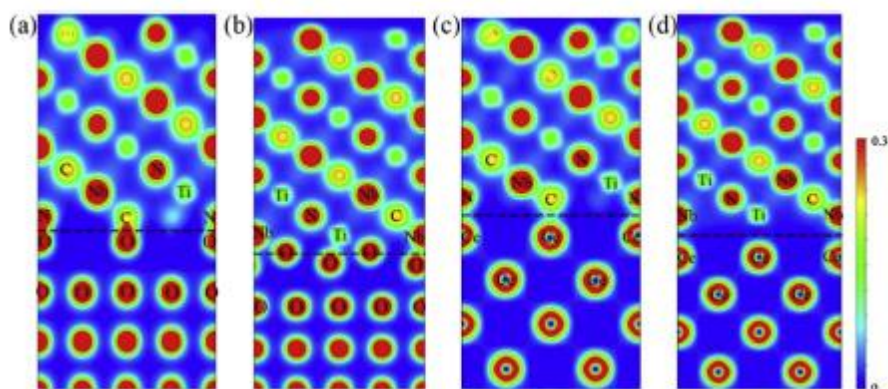
Fig. 10. Charge density distribution of (001) slices of CeO2(100)/Ti3NbCN3 (111) interfaces. (a) O-CN model; (b) O-TiNb model; (c) Ce-CN model; (d) Ce-TiNb model.
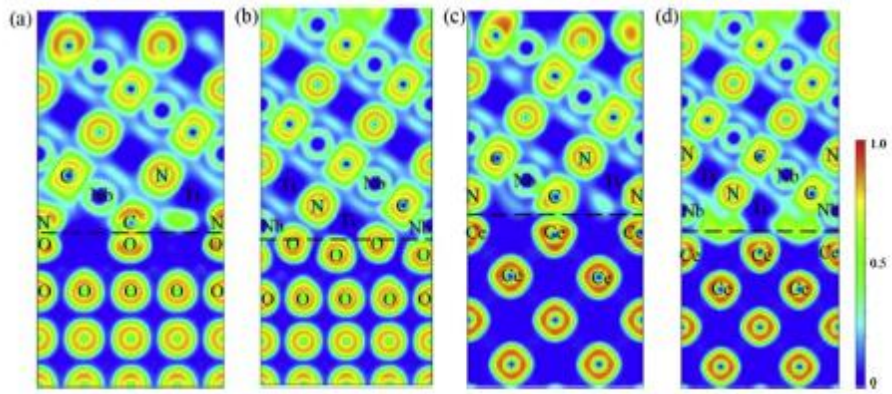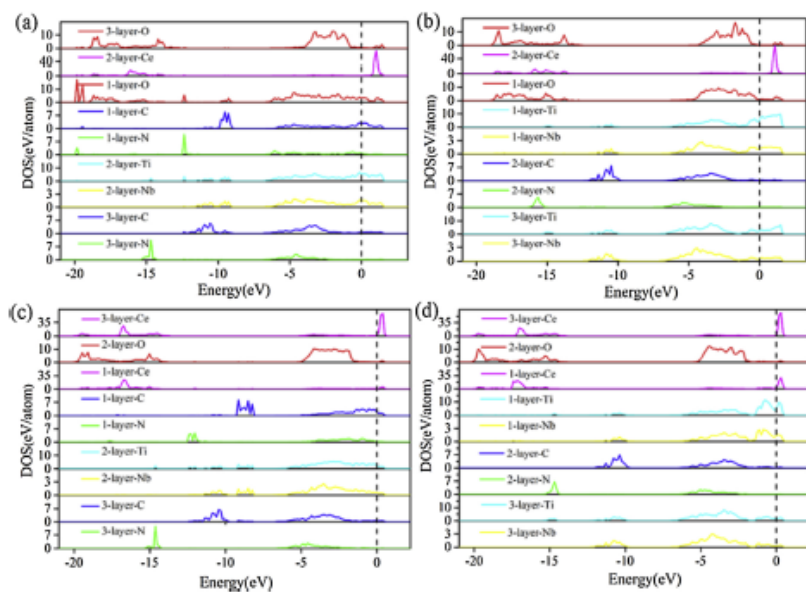
Fig. 11. ELF maps of (001) slices of CeO2(100)/Ti3NbCN3 (111) interfaces. (a) O-CN model; (b) O-TiNb model; (c) Ce-CN model; (d) Ce-TiNb model.

Fig. 12. PDOS of CeO2(100)/Ti3NbCN3 (111) interfaces. (a) O-CN interfaces; (b) O-TiNb interfaces;(c) Ce-CN interfaces; (d) Ce-TiNb interfaces.
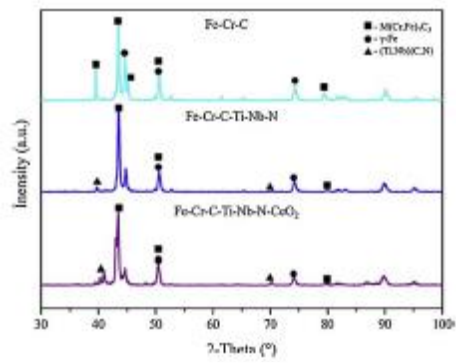
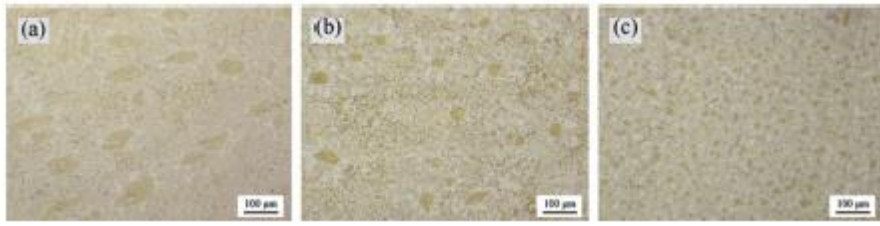**Fig. 13.** X-ray diffraction patterns of three coatings.

Fig. 14. Microstructure of three coatings. (a) Fe-Cr-C coating; (b) Fe-Cr-C-Ti-Nb-N coating; (c) Fe-Cr-C-Ti-Nb-*N*-CeO2 coating.
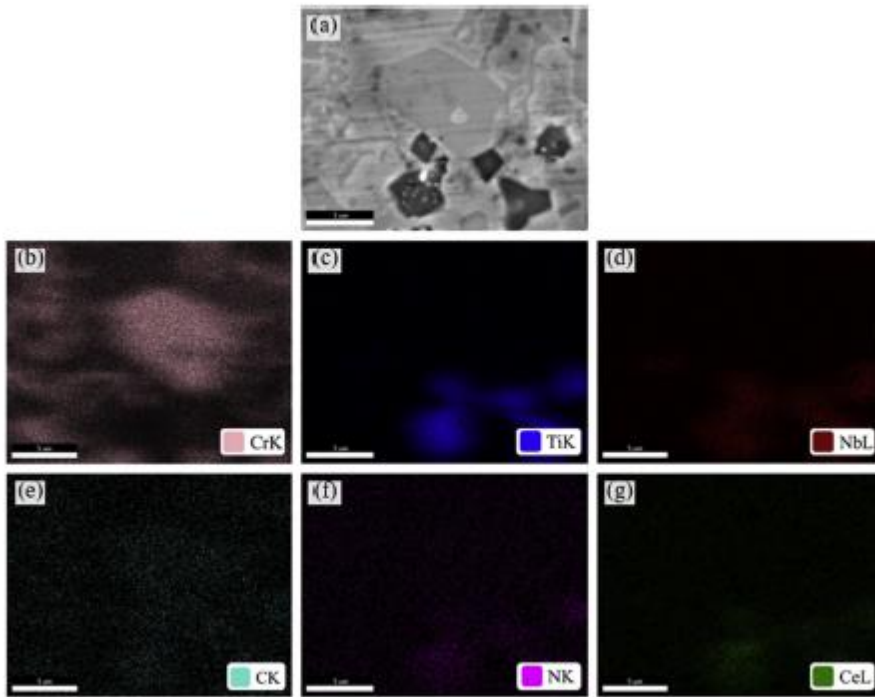
Fig. 15. Microstructure and element distribution maps of hypereutectic Fe-Cr-C-Ti-Nb-N-CeO2 coating. (a) Microstructure; (b) Element distribution of Cr; (c) Ti; (d) Nb;(e) C; (f) N; (g) Ce.